ACS APPLIED MATERIALS & INTERFACES

Research Article

Cite This: ACS Appl. Mater. Interfaces 2018, 10, 23529−23538

www.acsami.org

Scalable Synthesis of Biodegradable Black Mesoporous Silicon Nanoparticles for Highly Efficient Photothermal Therapy

Wujun Xu,[*,†,▽] Konstantin Tamarov,[†,∥,▽] Li Fan,[*,⊥] Sari Granroth,[#] Jimi Rantanen,[†] Tuomo Nissinen,[†] Sirpa Peräniemi,[‡] Oskari Uski,[§] Maija-Riitta Hirvonen,[§] and Vesa-Pekka Lehto[*,†]

[†]Department of Applied Physics, [‡]School of Pharmacy, and [§]Department of Environmental and Biological Sciences, University of Eastern Finland, 70211 Kuopio, Finland

[∥]Faculty of Physics, M. V. Lomonosov Moscow State University, 119991 Moscow, Russia

[⊥]Department of Pharmaceutical analysis, School of Pharmacy, and The State Key Laboratory of Cancer Biology (CBSKL), Fourth Military Medical University, 169th Changle West Road, 710032 Xi'an, Shaanxi, China

[#]Department of Physics and Astronomy, University of Turku, 20014 Turku, Finland

Supporting Information

ABSTRACT: Porous silicon (PSi) has attracted wide interest as a potential material for various fields of nanomedicine. However, until now, the application of PSi in photothermal therapy has not been successful due to its low photothermal conversion efficiency. In the present study, biodegradable black PSi (BPSi) nanoparticles were designed and prepared via a high-yield and simple reaction. The PSi nanoparticles possessed a low band gap of 1.34 eV, a high extinction coefficient of 13.2 L/g/cm at 808 nm, a high photothermal conversion efficiency of 33.6%, good photostability, and a large surface area. The nanoparticles had not only excellent photothermal properties surpassing most of the present inorganic photothermal conversion agents (PCAs) but they also displayed good biodegradability, a common problem encountered with the inorganic PCAs. The functionality of the BPSi nanoparticles in photothermal therapy was verified in tumor-bearing mice in vivo. These results showed clearly that the photothermal treatment was highly efficient to inhibit tumor growth. The designed PCA material of BPSi is robust, easy to prepare, biocompatible, and therapeutically extremely efficient and it can be integrated with several other functionalities on the basis of simple silicon chemistry.

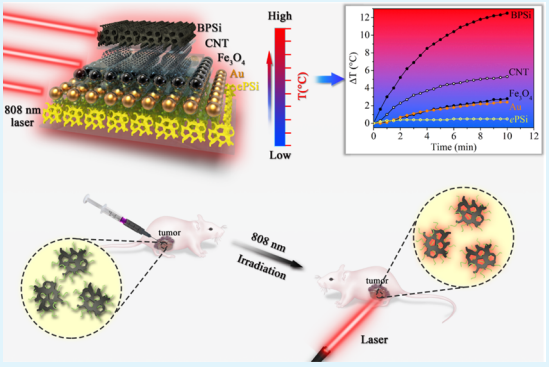

KEYWORDS: *porous silicon, high yield, biodegradability, photothermal treatment, cancer therapy*

INTRODUCTION

Photothermal therapy (PTT) is an attractive approach to treat various tumors.[1−4] Photothermal conversion agents (PCAs) absorb and convert light into heat, resulting in rapid and local ablation of cancerous cells. Near-infrared (NIR, 650−900 nm) light is generally utilized to achieve deep tissue penetration as well as to minimize the heating of nontarget tissues.[4] Many types of PCAs, including organic compounds[5−7] and inorganic materials,[2,8] have been developed for PTT applications. Organic PCAs such as indocyanine green have shown promising photothermal features and good biocompatibilities. However, these materials often suffer from photobleaching and low photothermal conversion efficiency. On the other hand, inorganic PCAs such as carbon nanotubes (CNTs),[9] graphene,[10] gold,[11−13] and metal sulfides,[14,15] commonly show both good photothermal conversion and excellent photostability. One drawback associated with all of these inorganic PCAs is that they typically degrade very slowly in biological conditions. This feature has aroused concerns about safety and biocompatibility, especially since it may be accompanied by the accumulation of heavy metals from some metal sulfides. Therefore, the development of novel PCAs combining all desired positive features is highly needed.

Mesoporous silicon (PSi) has attracted considerable attention in drug delivery due to its good biocompatibility, high surface area, large pore volume, and controllable pore diameter.[16,17] Moreover, PSi is biodegradable and its surface chemistry can be easily tailored for further functionalizations. The application of PSi in PTT has been studied previously,[18,19] in which the PSi was prepared through electrochemical etching (ePSi). However, the photothermal conversion efficiency of ePSi was much lower than that of the commonly utilized PCAs like gold and carbon-based nanomaterials.[20,21] Either a very high sample concentration of PSi (>0.7 mg/mL) or a high-power NIR laser was needed to achieve a therapeutic level of PTT.[17] Furthermore, the method to prepare ePSi was both

Received: March 20, 2018
Accepted: June 15, 2018
Published: June 15, 2018

DOI: 10.1021/acsami.8b04557
ACS Appl. Mater. Interfaces 2018, 10, 23529−23538

expensive and unecological and in addition, the production yield of these ePSi nanoparticles was rather low (less than 30%) partly due to the corrosive nature of the electrochemical process that generates pores by dissolving silicon with a large amount of toxic hydrofluoric acid (HF). Some efforts have been made to prepare PSi in an affordable manner, e.g., through a magnesiothermic reduction process[22,23] and Na−K alloy reduction.[24] However, none of these reported PSi nanomaterials have had a sufficiently high photothermal efficiency that they could be applied in efficient PTT.

In the present study, a new type of black PSi (BPSi) nanoparticles was designed to be produced with a simple synthesis based on sodium silicide (NaSi). The synthesis method is inexpensive and it achieves a high yield. The prepared BPSi has a high surface area, good biodegradability, and an excellent photothermal conversion efficiency. BPSi is more efficient in converting NIR light (808 nm) into heat than the selected inorganic PCAs such as gold nanoparticles (diameter = 5.0 nm), Fe_3O_4 (diameter = 10 nm), and single-wall carbon nanotubes. The application of BPSi in PTT for cancer therapy is demonstrated in both in vitro cell experiments and in vivo animal trials.

MATERIALS AND METHODS

Materials. Sodium silicide (NaSi) and Si wafers (diameter 20 cm, p+ (100), 0.01−0.02 Ω cm) were provided by SiGNa Chemistry Inc. and Okmetic Inc., respectively. Ammonium bromide (NH_4Br, 99%), sodium bromide (NaBr, 99%), toluene (anhydrous, 99.8%), (3-aminopropyl)triethoxysilane (APTES), isopropyl alcohol (IPA), and hydrochloric acid (HCl, 37%) were bought from Sigma-Aldrich. Phosphate buffer saline (PBS, pH = 7.4) was bought from VWR. Methoxy-poly(ethylene glycol) (PEG)-silane (0.5 kDa) and methoxy-PEG-silane (2 kDa) were bought from Fluorochem Ltd. and Laysan Bio Inc. separately. The CellTiter Glo cell luminescent viability assay was purchased from Promega. All reagents were used directly as received.

Preparation of BPSi and ePSi Nanoparticles. NaSi, ammonium salt, and NaBr (NaSi/NH_4Br/NaBr of 1:4:4, w/w/w) were ground in a glovebox with an Ar atmosphere. The salt of NaBr is used since it achieves a better dispersion of NaSi and NH_4Br. They were allowed to react in a tube oven under a N_2 atmosphere at 240 °C for 5 h according to eq 1

$$NaSi + NH_4Br \rightarrow NaBr + NH_3 + Si/H + H_2 \quad (1)$$

After being cooled down to ambient temperature, the obtained microparticles were purified by rinsing with 0.5 M HCl and 1.0 M HF solutions separately. The microparticles were ball-milled in ethanol at 1000 rpm for 15 min, and the BPSi nanoparticles with desired diameter were collected via adjusting the centrifugation speed. The concentration of the nanoparticles in the suspension was determined by measuring the mass of the nanoparticles after drying a precisely measured volume of the nanoparticle suspension.

The ePSi nanoparticles were used as reference samples. They were prepared via ball-milling of ePSi films, which were produced through electrochemical HF-etching of Si wafer, as reported previously.[25]

Dual-PEGylation of BPSi. The BPSi nanoparticles were oxidized to generate Si−OH groups to further functionalize the surface with PEG-silane, according to the method described previously.[25] Accordingly, two PEG-silanes with different lengths of carbon chains (0.5 and 2.0 kDa) were dissolved in toluene. The nanoparticles were mixed with the above solution and reacted at 110 °C under a N_2 atmosphere for 1 day.[26] Finally, the nanoparticles were rinsed with ethanol three times to remove unreacted PEG-silanes on the surface. The BPSi nanoparticles with dual-PEGylation were denoted as DPEG-BPSi. Fresh DPEG-BPSi nanoparticles were used directly for physicochemical characterizations and in vitro tests. For in vivo experiments, the nanoparticles were lyophilized in 4% mannitol aqueous solution and stored at +4 °C.

Fluorescent Labeling. Fifty milligrams of BPSi or DPEG-BPSi nanoparticles were reacted with 20 μL of APTES in 5 mL of IPA at 60 °C for 2 h. The amine-modified nanoparticles were washed with ethanol and then reacted with fluorescein isothiocyanate (FITC) in ethanol overnight at ambient temperature. Finally, the residual amine groups were passivated with succinic anhydride in dimethyl sulfoxide to convert the positive surface charge to negative charge, avoiding the nonspecific cell interaction with the positively charged amine surface.

Characterizations. X-ray diffraction (XRD) was utilized to analyze the crystal structure of the prepared nanoparticles. The porous parameters of the nanoparticles were evaluated with N_2 adsorption/desorption experiments (Tristar II 3020, Micromeritics) at 77 K. The specific surface area of samples was calculated using the multiple-point Brunauer−Emmett−Teller (BET) method, and the pore diameter distribution was analyzed according to the Barrett−Joyner−Halenda (BJH) theory. The hydrodynamic diameters of the nanoparticles were measured with Malvern Zetasizer Nano ZS utilizing the method of dynamic laser scattering (DLS). The morphology of the nanoparticles was measured with high-resolution transmission electron microscopy (HR-TEM) (JEOL JEM2100F). A few drops of sample dispersion were dried on 200 mesh copper grids with Formvar films for TEM analysis. The BPSi slices prepared from BPSi microparticles were imaged with TEM to see the porous structure. Prior to the image process, the BPSi samples were embedded with LX-112 resin polymer at 60 °C and the cast samples were cut with microtome (Leica EM UC7, Diatome diamond knife ultra 45°) in slices of ca. 70 nm thickness. PerkinElmer PHI 5400 was used for X-ray photoelectron spectroscopy (XPS) measurements. The photoemission spectra of Si 2p were collected with Mg Kα radiation (1253.6 eV). The fitting procedure was done using spectral analysis by Curve Fitting Macro package for Igor Pro. The impurity of sodium content in the samples was analyzed with an inductively coupled plasma mass spectrometer (ICP-MS) (Elan 6100, PerkinElmer). The dried nanoparticles were digested in a microwave dissolution oven with the following acids: nitric acid, hydrochloric acid, hydrofluoric acid, and boric acid.

Heating kinetics of various nanoparticle suspensions were tested under continuous IR laser radiation (PL-808-1000, SKY Laser). One milliliter of suspension was placed into DLS cuvettes and irradiated with 808 nm laser wavelength (1.0 W power). The temperature change of the suspension was monitored with the thermocouple (type K) immersed into the suspension. The evaluated nanoparticles were Au nanoparticles, Fe_3O_4, carbon nanotubes (CNTs), ePSi, and BPSi. The Au nanoparticles and CNTs were purchased from Sigma-Aldrich and Timesnano, respectively. The Fe_3O_4 nanoparticles were prepared according to the method published before.[27]

Degradation tests of BPSi and DPEG-BPSi were carried out by incubating the nanoparticle in PBS (75 μg/mL) at 37 °C. At predetermined time points, 2.0 mL of samples were withdrawn and centrifuged to separate the NPs. The supernatants were analyzed with the ICP-MS to determine the concentration of the dissolved Si.

Cell Viability. CT 26 cells were cultured in Dulbecco's modified Eagle's medium (Sigma-Aldrich) and RPMI-1640 (Biowest) supplemented with 10% fetal bovine serum (Sigma-Aldrich), 1% L-glutamine (Sigma-Aldrich), and 1% antibiotic cocktail (Antibiotic-Antimycotic Solution, Corning). The luminescence from CellTiter Glo (Promega Corp.) assay was measured for viability evaluation.

A total of 10^4 cells per well in 100 μL of culture medium in a 96-well plate was allowed to attach for 20 h. Then, predetermined concentrations of BPSi or DPEG-BPSi nanoparticles in the culture medium were added. The cells were incubated with the nanoparticles for 4 h, after which the cells were washed three times with culture medium to remove free particles. Subsequently, they were incubated for 44 h prior to performing the viability assay.

Cell Uptake. CT 26 cells were cultured on the 8-well plate and incubated with 50 μg/mL FITC-labeled BPSi or DPEG-BPSi nanoparticles for 10 min, 1.0 h, 4.0 h, and 24 h. The cells were

DOI: 10.1021/acsami.8b04557
ACS Appl. Mater. Interfaces 2018, 10, 23529−23538

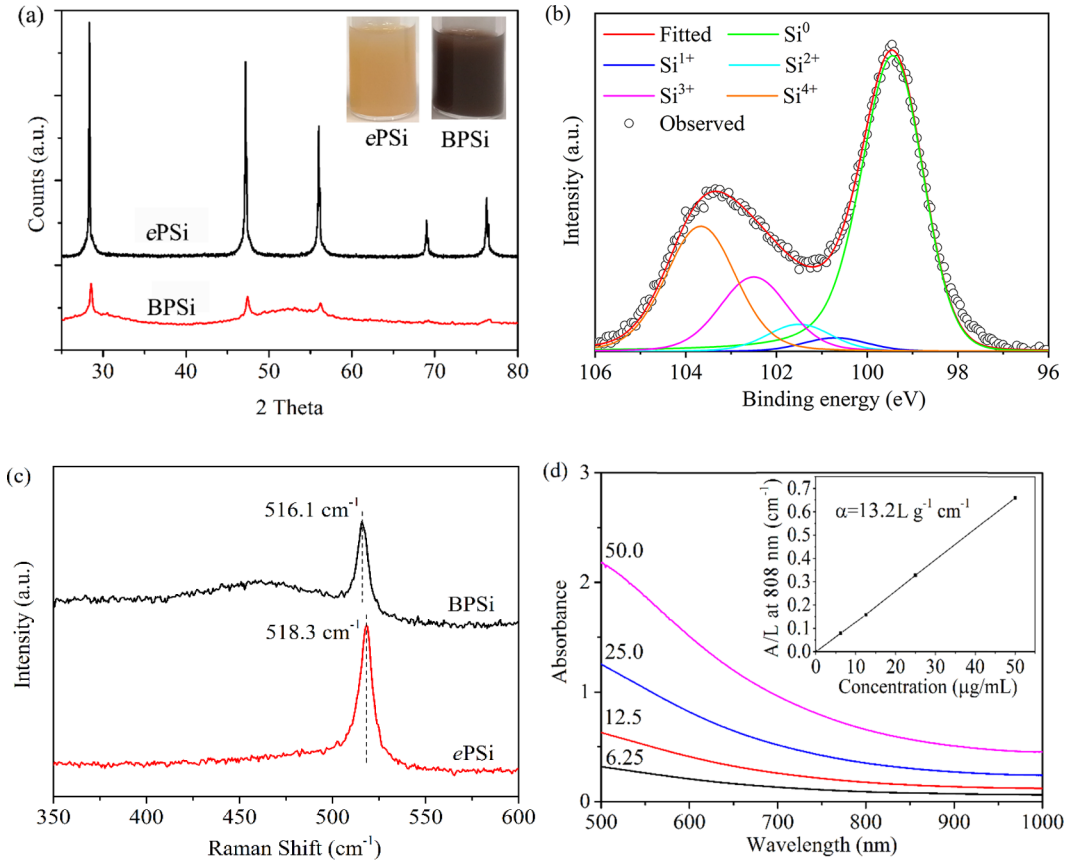

Figure 1. Characterization of nanoparticles: (a) XRD patterns and photographs of the sample dispersions (inset) of ePSi and BPSi, (b) XPS spectra of BPSi, (c) Raman spectra of ePSi and BPSi, (d) UV−vis absorption spectra of BPSi dispersions with different concentrations (6.25, 12.5, 25.0, and 50.0 μg/mL). The inset is the normalized absorbance intensity (A) divided by the length (L) of the cuvette at 808 nm.

washed with PBS and cell medium three times separately. The cells were labeled with CellMask prior to fluorescence image.

In Vitro PTT for Ablation of Cancer Cells. A specific setup was constructed to measure the temperature of the cell medium and to control the power of the laser (Figure S1, Supporting Information). The laser was mounted in a cell incubator (Sanyo MCO-19 AIC (UV)) vertically in such a way that the beam was directly irradiating the cells in one of the wells (96-well plate). The diameter of the laser beam was equal to the diameter of the well. An infrared sensor, connected to a microcontroller, was attached on the side of the laser, and this was directed to the well to read the temperature at a rate of 10 measurements per second. The microcontroller averaged five subsequent temperature reads from the sensor and sent the data to the computer twice every minute. The sensor was calibrated with a thermocouple thermometer. The data from the sensor was used to control the laser power by changing the electrical current from a power source (Agilent N5768A) through a homemade C# program. The program received the temperatures and using proportional−integral−derivative controller calculated the electrical current to control the power source. This kind of control made it possible to heat the cell medium up to a certain temperature and maintain it at the desired level with high accuracy.

A total of 2×10^4 cells per well (96-well plate) in 100 μL of culture medium were allowed to attach for 20 h. Then, the culture medium was replaced with 200 μL of culture medium containing predetermined concentrations of DPEG-BPSi nanoparticles. Subsequently, the cells were incubated with the nanoparticles for 1 h to equilibrate to the medium temperature of 37 °C in the incubator. Subsequently, the cells were irradiated with the IR laser for predetermined time intervals. After the laser treatment, the nanoparticles were removed by replacing the cell culture media with a fresh one and the incubation was continued for 12 h. Cell viability was examined with CellTiter Glo assay, and the apoptotic and necrotic cells were analyzed with flow cytometry using FAM FLICA Caspase-3/7 Kit (Immunochemistry Technologies LLC) to stain apoptotic cells and DRAQ7 (Abcam) to stain necrotic cells. The apoptotic and necrotic cells were measured to evaluate the mechanism of heat-induced cell death.

In Vivo Assessment of Antitumor Effect in Tumor Xenograft. All animal experiments were approved by the Animal Experiment Administration Committee of the Fourth Military Medical University, China. Mouse colonic epithelial CT 26 cells (5 × 106 cells, total volume 0.1 mL) were injected into mice (Female BALB/C nude mice, 4−6 weeks) legs subcutaneously to establish tumors. When the diameters of the tumors were above 2.0 mm as measured by calipers, the mice-bearing tumor were randomly divided into six groups (five mice/group): saline control (0.1 mL), saline with irradiation (saline + laser), 0.5 mg/mL DPEG-BPSi (DPEG-BPSi-0.5), 1.0 mg/mL DPEG-BPSi (DPEG-BPSi-1.0), DPEG-BPSi-0.5 + laser, and DPEG-BPSi-1.0 + laser. The freeze-dried nanoparticles were washed with saline to remove any excess mannitol prior to animal test. The nanoparticles redispersed in saline solution were administered as an intratumoral injection. Every mouse in the groups of saline + laser, DPEG-BPSi-0.5 + laser, and DPEG-BPSi-1.0 + laser was treated with laser irradiation (808 nm, 1.0 W/cm^2) for 10 min immediately after the injections. An infrared detector was used to determine the temperature of the heating regime. The whole observation was conducted to verify that the laser itself did not overheat and damage the skin of the animals. All animals were monitored for activity, physical condition, body weight, and tumor growth. Body weight and tumor size of each mouse were measured and recorded every other day until sacrifice. Before sacrifice, the animals were anaesthetized with an intraperitoneal injection of pentobarbital sodium (16 mg/mL, 0.1 mL/mice). The mass of the tumor was weighed and major organs

DOI: 10.1021/acsami.8b04557
ACS Appl. Mater. Interfaces 2018, 10, 23529−23538

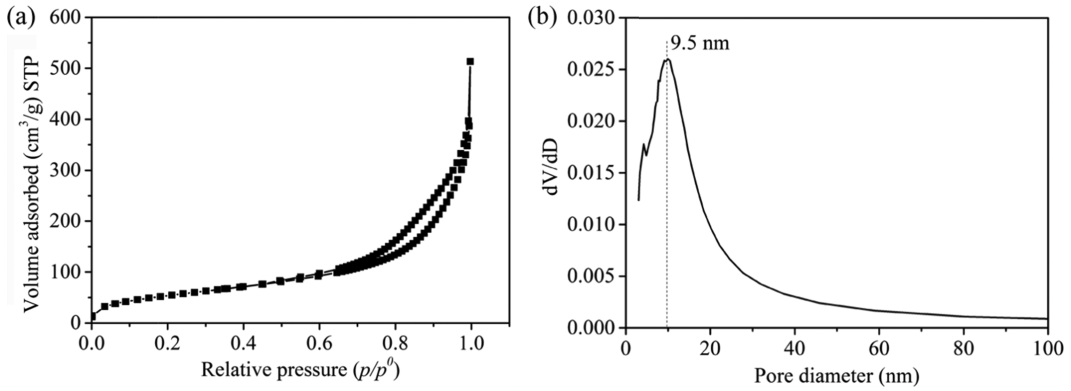

Figure 2. (a) N_2 adsorption and desorption isotherm and (b) pore diameter distribution of BPSi. The data from the desorption branch was used to analyze the pore diameter distribution according to the Barrett–Joyner–Halenda (BJH) theory.

were collected after sacrifice for further analysis. All of the data are reported as the means ± standard deviations (SDs).

Hematoxylin and Eosin (H&E) Assay. The major organs were fixed in 4% paraformaldehyde at 4 °C overnight and embedded in paraffin for preparing 5 μm thick sections, followed by H&E (haematoxylin/eosin, Beyotime, China) study. Histology and morphology of major organs were observed under the Eclipse E800 microscope (Nikon, Japan). Images were randomly taken from 400× in each section.

Statistical Analysis. Data were analyzed by one-way analysis of variance (ANOVA) statistical analysis with Sidak's multiple comparisons test (Graphpad Prism 5.01 software) to determine the differences between groups. A significant difference was judged by $P < 0.05$.

RESULTS AND DISCUSSION

Physicochemical Characterizations. The reaction between NaSi and NH_4Br has been developed as a low-cost method to prepare ultra-small silicon nanoparticles (ca. 5.0 nm in diameter) in a high-boiling-point organic solvent.[28] NaBr, NH_3, and H_2 are the byproducts of the reaction. The ultra-small silicon nanoparticles were monodispersed in the organic solvent after the reaction. In the present study, we hypothesized that the small silicon nanoparticles would aggregate to form a mesoporous silicon matrix in a solid-phase reaction, in which the NaBr salt could act as the pore template while NH_3 and H_2 were evaporated. After the NaBr had been washed away, silicon microparticles with nanosized pores were obtained. The yield was 80–90%, which is substantially higher than that of ePSi prepared with the HF-etching method. Finally, the BPSi nanoparticles with a mean diameter of 156 nm were prepared with ball-milling (Figure S2, Supporting Information). The crystal structures of the prepared nanoparticles were characterized with XRD (Figure 1a). The diffraction peaks of both BPSi and ePSi were indexed as diamond-like (cubic) Si phase (JCPDS card no. 27-1402).[29] The crystallite size of BPSi nanoparticles is 17 nm, as calculated by the Debye–Scherrer equation. The insets of Figure 1a are photographs of BPSi and ePSi as aqueous dispersions (75 μg/mL): the BPSi dispersion appeared black, whereas the ePSi dispersion appeared yellow. The binding energies of Si 2p lines of BPSi were found at 99.5, 100.7, 101.5, 102.5, and 103.5 eV, corresponding to Si^0, Si^{1+} (Si_2O), Si^{2+} (SiO), Si^{3+} (Si_2O_3), and Si^{4+} (SiO_2), respectively (Figure 1b).[30,31] There were approx. 54% of elemental Si and 46% of oxidized silicon (SiO_x, $0 < x \leq 2$) on the surface of the BPSi nanoparticles on the basis of the fitted relative areas of the peaks (Table S1). The corresponding values for the ePSi nanoparticles were approx. 64 and 36% for elemental Si and oxidized silicon, respectively (Figure S3a, Supporting Information). The data obtained from their Raman spectra (Figure 1c) confirmed these observations in XPS analyses. The broad peak shoulder between 400 and 500 cm^{-1} is attributed to amorphous SiO_x ($0 < x \leq 2$).[24] The location of the Si peak in BPSi was blue-shifted to 516.1 cm^{-1} compared with 518.3 cm^{-1} of ePSi and 521.4 cm^{-1} of bulk silicon wafer (Figure S3b, Supporting Information).

The BPSi nanoparticles display a broad absorption band in the NIR region (Figure 1d), which is similar to that of other PCAs such as graphene oxide.[21] The linear relation of absorption intensity over the characteristic length of the cuvette (A/L) at 808 nm is shown in the inset of Figure 1d. The mass extinction coefficient (α) of BPSi obtained at 808 nm was 13.2 L/g/cm according to the Lambert–Beer Law. The coefficient is 5.5 times higher than that of ePSi (Figure S3c, Supporting Information). The band gap of the BPSi nanoparticles was 1.34 eV according to the Kubelka–Munk model (Figure S4, Supporting Information).[32] The corresponding value of ePSi was 2.51 eV. The difference of the band gap is probably due to the presence of a low amount of Na impurity (0.6%) in BPSi according to the ICP-MS analysis. The band gap of 1.34 eV in BPSi corresponds to the wavelength of 925 nm, and therefore the light of shorter wavelengths such as 808 nm can be efficiently absorbed by BPSi nanoparticles through the excitation of electrons into the conduction band. On the contrary, the band gap of 2.51 eV in ePSi is equivalent to 494 nm, resulting in the low infrared absorption by ePSi.

The nitrogen adsorption/desorption isotherms of BPSi (Figure 2a) were of the IV isotherm type with H1 hysteresis, indicating the presence of mesoporous structure in BPSi. The Brunauer–Emmett–Teller (BET) surface area of BPSi was 120 m^2/g, the pore volume was 0.42 cm^3/g, and porosity was 49% (Supporting Information). The pore diameter was around 9.5 nm according to the Barrett–Joyner–Halenda (BJH) theory (Figure 2b), which was consistent with the result in TEM images of BPSi microparticle slices (Figure S5, Supporting Information). The wormlike pore structure with the diameter in the range of 8.0–15.0 nm was observed. The BPSi nanoparticles had irregular morphology (Figure S6a, Supporting Information), and the atomic lattice planes were clearly observed in the HR-TEM image (Figure S6b, Supporting Information). The lattice fringe of 0.31 is

DOI: 10.1021/acsami.8b04557
ACS Appl. Mater. Interfaces 2018, 10, 23529–23538

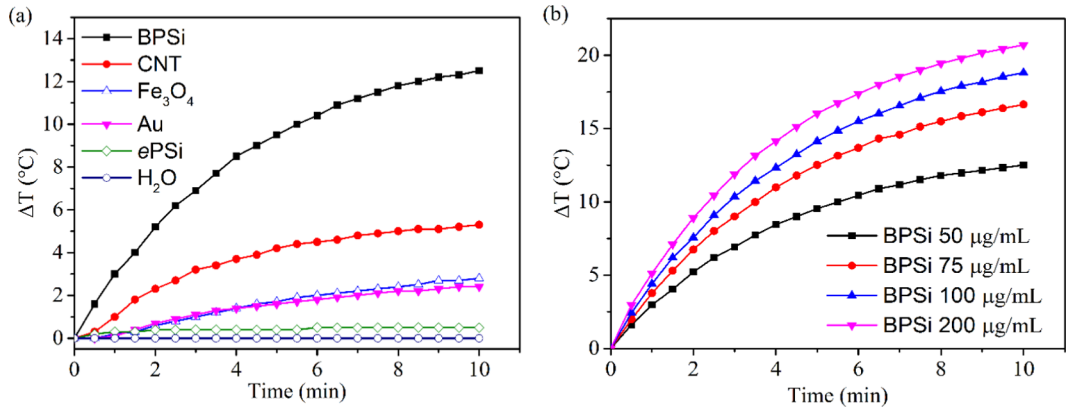

Figure 3. Photothermal heating curves of sample dispersions under laser irradiation (808 nm): (a) different nanoparticles with the concentration of 50 μg/mL and (b) BPSi nanoparticles with different concentrations.

consistent with the *d*-spacing value of the (111) plane of cubic silicon structure.[24] The crystallite size of the BPSi nanoparticles ranges from 10 to 20 nm, as shown in the HR-TEM image, which is in accordance with the calculation from the XRD measurement.

The comparison of photothermal property of BPSi with other nanoparticles was conducted using an 808 nm NIR laser with the power of 1 W for 10 min. The temperature of the 50 μg/mL BPSi dispersion increased by 12.5 °C, which was 25 times higher than that of ePSi (0.48 °C) under identical experiment conditions (Figure 3a). Moreover, the BPSi nanoparticles underwent a more efficient photothermal conversion than the selected photothermal conversion agents, including gold nanoparticles (diameter = 5 nm), single-wall carbon nanotube, and Fe_3O_4 (diameter = 10 nm). The photothermal heating performance of BPSi nanoparticles was compared with gold nanoparticles of different sizes. With the increase of the particle diameter, the heating performance of gold nanoparticles decreased (Figure S7a, Supporting Information). The effect of BPSi particle concentration on the photothermal heating performance was studied. The temperature elevation of the BPSi dispersion increased with the increasing nanoparticle concentration (Figure 3b). The photostability of the BPSi nanoparticles was evaluated by repeating five cycles of heating (laser on)-cooling (laser off) process. There was no significant difference in the temperature elevation in the cycled tests, demonstrating the excellent photothermal stability of the BPSi nanoparticles (Figure S7b, Supporting Information). The photothermal conversion efficiency (η) of the BPSi nanoparticles was approx. 33.6%, calculated according to the reported method (Supporting Information).[33,34] This value is higher than the corresponding values for other widely used PCAs, like Au (nanoshells 13%, nanorods 21%),[35] Fe/Fe_3O_4 (20.3%),[36] black phosphorus quantum dots (24.8%),[20] and Bi_2S_3 (28.1%).[14] Nevertheless, there was around 5% decrease in the photothermal conversion efficiency due to the PEGylation (Figure S7c, Supporting Information). The surface of the nanoparticles was partially oxidized to produce Si−OH groups that reacted with PEG-silane for the PEGylation. The oxidation of the surface compromised the heating performance a bit.

In Vitro Biological Studies. Surface PEGylation is commonly utilized to improve the biocompatibility of nanoparticles.[37] In the present study, dual-PEGs with different lengths of carbon chains were functionalized on the surface of BPSi nanoparticles. This dual-PEGylation method has been verified to successfully enhance the biocompatibility in vitro and in vivo in our previous study.[26] Around 12% w/w of PEGs was grafted onto the surface of the dual-PEGylated BPSi (DPEG-BPSi) nanoparticles (Figure S8, Supporting Information). The change of the ζ-potential from −18.5 to +2.8 mV also indicated that the surface dual-PEGylation was successful (Figure S8). The biological stability of the BPSi nanoparticles before and after PEGylation was examined in PBS (pH = 7.4) at 37 °C. The plain BPSi nanoparticles had poor stability in PBS, and their hydrodynamic diameter increased from 156 nm to the micrometer range in 1.0 h (Figure 4a). In contrast, the colloidal stability of the nanoparticles was significantly enhanced because of the dual-PEGylation. The DPEG-BPSi was stable in PBS at 37 °C for over 24 h.

The biodegradation product of PSi-based nanoparticles, orthosilicic acid ($Si(OH)_4$), is the form of silicon predominantly absorbed by humans and is naturally found in numerous tissues.[38] The biodegradation of the BPSi and DPEG-BPSi nanoparticles was carried out in PBS by monitoring the Si concentration in the solution (Figure 4b). The increased half-life from 0.8 to 3.0 days due to the dual-PEGylation was consistent with the previous study.[26] Thus, the BPSi nanoparticles are biodegradable and their biodegradability is tunable with surface functionalization. On the other hand, the laser heating for 10 min did not significantly change the biodegradation rate of DPEG-BPSi nanoparticles (Figure 4b). Since most inorganic PCAs are prepared from Au, carbon-based graphene/nanotubes, transition-metal carbides, or sulfides, they do not degrade in biological fluids and their bio-resorption can take several weeks or even months.[39] Thus, the biodegradability is always an issue when applying these materials in nanomedicine.

The biocompatibility of the nanoparticles was evaluated with the CT 26 cancer cells (Figure S9a, Supporting Information). The plain BPSi nanoparticles exhibited good biocompatibility with the CT 26 cells if their concentration was below 200 μg/mL. With the increase of their concentration over 500 μg/mL, cytotoxicity was expressed to some extent. However, surface PEGylation improved the biocompatibility of the nanoparticles. The DPEG-BPSi nanoparticles did not show any significant signs of cytotoxicity to the CT 26 cells even at a concentration of 1.0 mg/mL.

The time-dependent uptake of the nanoparticles into the CT 26 cells was studied with fluorescent confocal microscope

DOI: 10.1021/acsami.8b04557
ACS Appl. Mater. Interfaces 2018, 10, 23529−23538

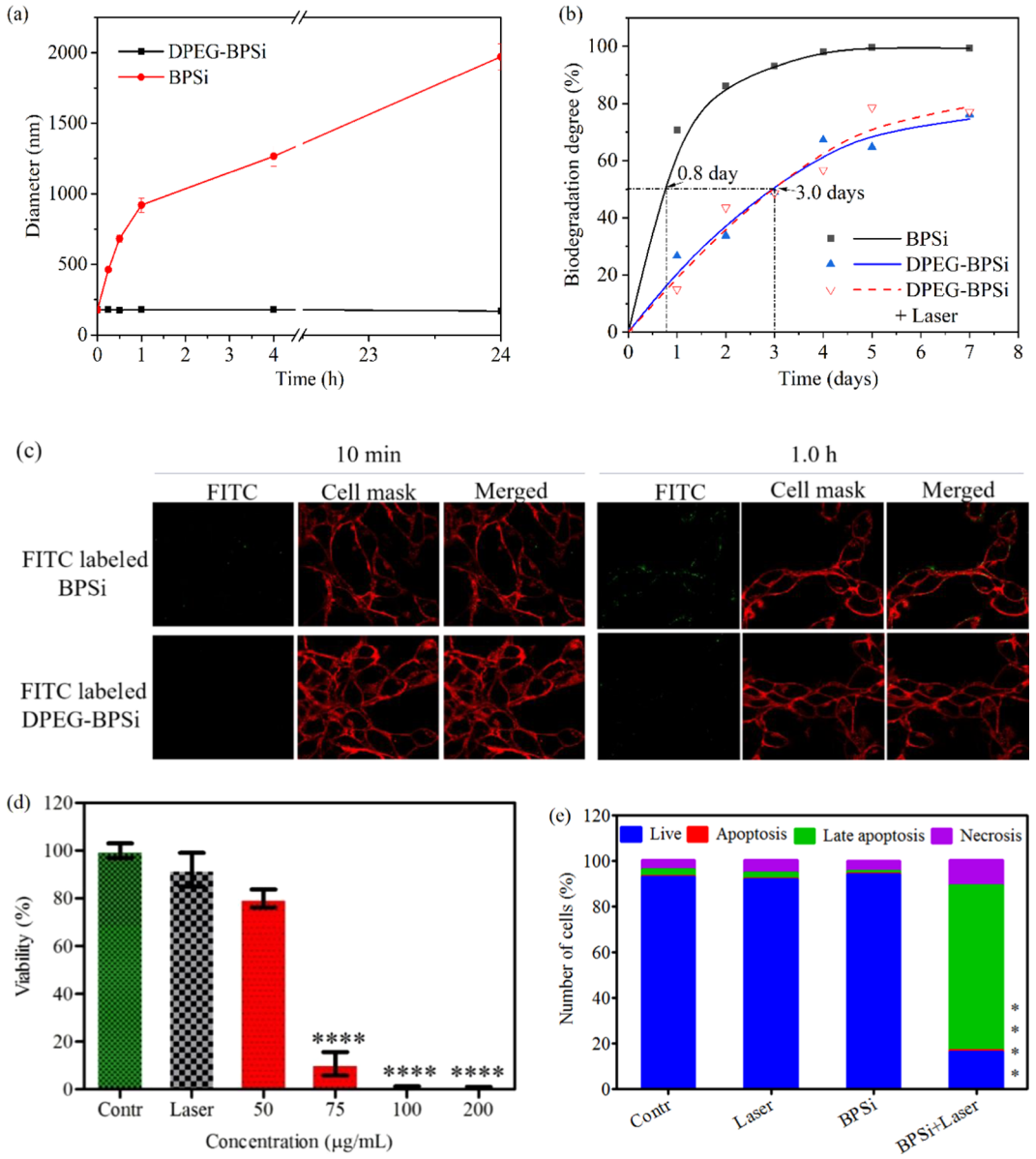

Figure 4. (a) Colloidal stability of nanoparticles in PBS. (b) Biodegradation tests of the BPSi and DPEG-BPSi nanoparticles in PBS with pH 7.4 at 37 °C for different time periods. The DPEG-BPSi nanoparticles were heated with the laser for 10 min before the biodegradation tests to study the effect of laser heating. (c) Fluorescent confocal microscope image on the uptake of BPSi and DPEG-BPSi nanoparticles into CT 26 cells after the incubation of 10 min and 1.0 h. (d) Viability of the CT 26 cells after photothermal treatments with different concentrations of DPEG-BPSi nanoparticles. The number of the samples per group was four. (e) The relative number of live, apoptotic, late apoptotic, and necrotic CT 26 cells after a 10 min laser heating of the medium with 75 μg/mL DPEG-BPSi nanoparticles followed by 12 h of incubation in nanoparticle-free media. The control (Contr) and laser (Laser) samples do not contain nanoparticles. Statistical analysis was done by one-way ANOVA: $P < 0.0001$ (****), as compared with the control group.

(Figure 4c and S9b, Supporting Information). There was no significant uptake of the DPEG-BPSi nanoparticles before the 4.0 h incubation with the cells. Some DPEG-BPSi nanoparticles were gradually internalized at the time point of 24.0 h. Nevertheless, it is evident that the DPEG-BPSi nanoparticles had much less cellular uptake than that of the control BPSi nanoparticles without PEG coating.

Motivated by the excellent biocompatibility and photothermal properties of the nanoparticles, the efficacy in photothermal treatment (PTT) was tested in vitro with CT 26 cells (Figure 4d). The PTT effect on the viability of CT 26 cells was observed to be dose dependent. When the laser was applied with the DPEG-BPSi dispersion of 75 μg/mL, most of the cells were killed. On the contrary, the laser heating without the nanoparticles did not cause any significant cell death. To further evaluate the cell death mechanism induced by the laser heating of 75 μg/mL nanoparticle dispersions, the cells were stained with apoptotic and necrotic dyes after the laser treatment. The results about photothermal cancer cell ablation from flow cytometry (Figures 4e and S10, Supporting Information) are in agreement with those from CellTiter Glo shown in Figure 4c. In addition to 16% of live cells, the cell death consisted of 1% apoptosis, 72% late apoptosis, and 11% necrosis. The cell necrosis increased from 5 to 11% in the group treated both with BPSi nanoparticles and laser irradiation, compared with the control groups with BPSi or

DOI: 10.1021/acsami.8b04557
ACS Appl. Mater. Interfaces 2018, 10, 23529−23538

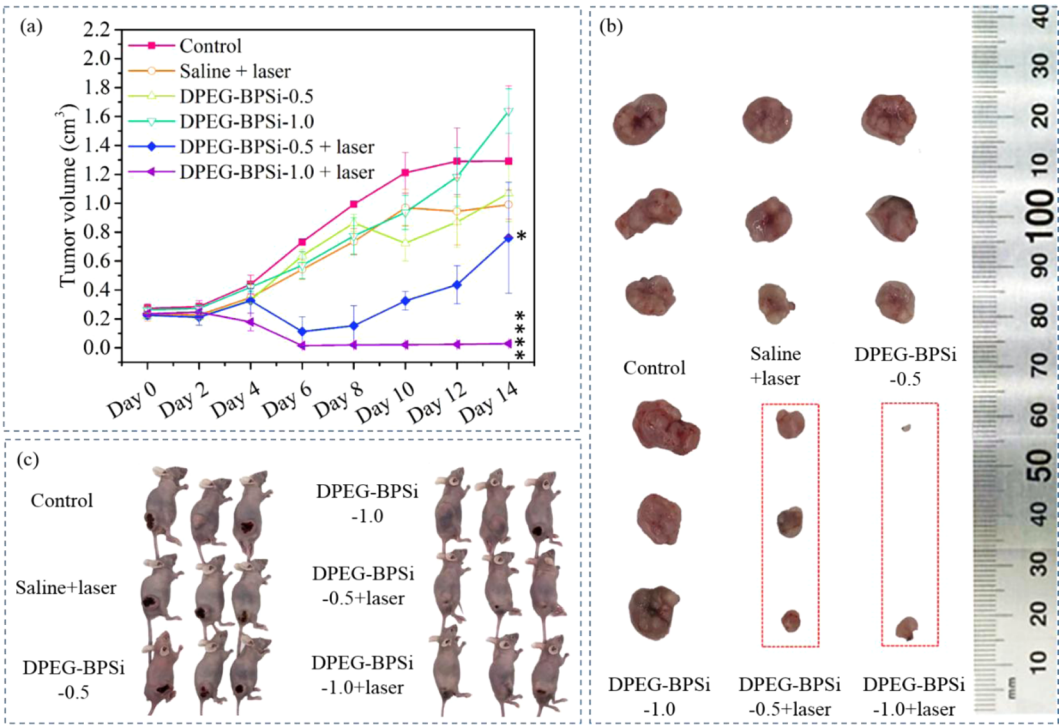

Figure 5. Antitumor effect of the DPEG-BPSi nanoparticles on nude mice bearing CT 26 tumors. (a) Values of tumor volume are expressed as mean ± SD (n = 5). (b) Dissected tumor tissues from the nude mice. (c) Photos of anaesthetized mice at day 14 after treatment. All tumor volume data at day 14 were analyzed by one-way ANOVA statistical analysis: $P < 0.05$ (*) and $P < 0.0001$ (****).

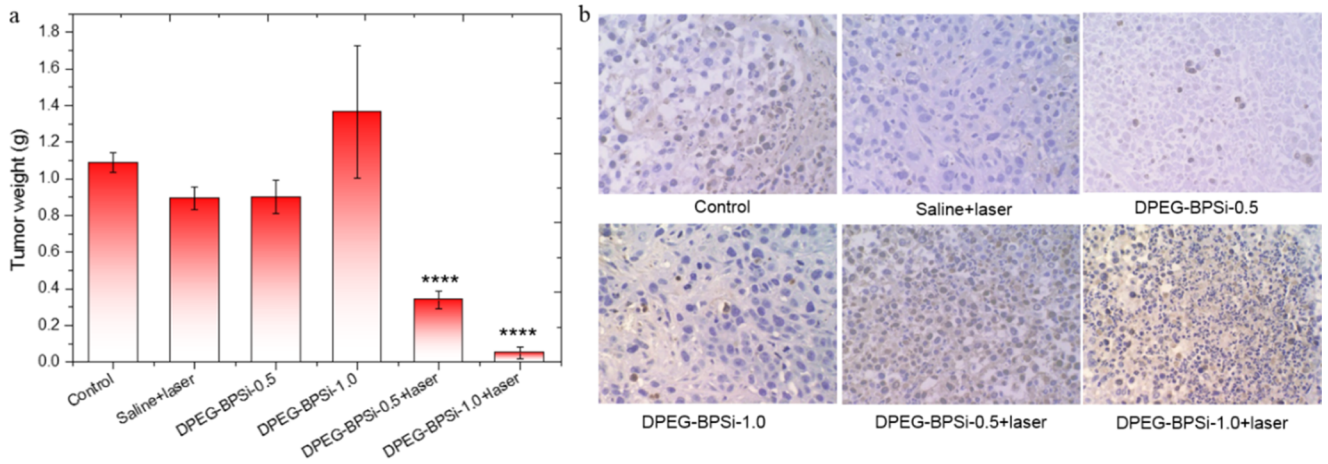

Figure 6. Antitumor effect of DPEG-BPSi with/without laser on nude mice bearing CT 26 cells subcutaneously was studied. (a) Values of tumor weight are expressed as mean ± SD (n = 5). (b) TUNEL assay of tumor biopsies in control and all treatment groups with/without irradiation. All tumor volume data at day 14 were analyzed by one-way ANOVA statistical analysis: $P < 0.0001$ (****).

laser only. According to the literature, the nanoparticles localized on the cell membrane were particularly effective to induce tumor cell necrosis under laser irradiation,[40] via making the membrane bleb and increasing membrane permeability. However, in the present study, the BPSi nanoparticles were mainly distributed in the extracellular environment during the laser irradiation. So the mechanism of cell necrosis is attributed to the hyperthermia itself, which can lead to both apoptosis at mild heating regimes and necrosis at higher temperatures,[41] indicated by the presence of caspases and membrane permeability (late apoptosis and necrosis in Figure 4e), respectively.

In Vivo Antitumor Tests. A tumor xenograft (CT 26 colon tumor) mouse model was used to evaluate the in vivo antitumor efficacy. The sample dispersions were administered as intratumoral injections. The nanoparticles with laser irradiation significantly delayed subcutaneous tumor growth, as demonstrated by the tumor volume evolution (Figure 5). In the absence of laser irradiation, the pure DPEG-BPSi nanoparticles did not show any antitumor activity. In the saline + laser treatment group, the temperature of tumor surface slightly increased from 37 to 40 °C. The tumor growth inhibition was also not obvious as compared to that in the control group. A significant inhibition of tumor growth was achieved when combining DPEG-BPSi nanoparticles with laser

DOI: 10.1021/acsami.8b04557
ACS Appl. Mater. Interfaces 2018, 10, 23529−23538

irradiation. Tumor volume growth in the mice groups treated with DPEG-BPSi-0.5 + laser and DPEG-BPSi-1.0 + laser was effectively suppressed for the first 8 days after the treatment. Even though there was tumor relapse after day 8 in the group with lower particle dose (DPEG-BPSi-0.5 + laser), the tumor growth in the group with higher particle dose (DPEG-BPSi-1.0 + laser) was continuously inhibited. At least 50% of tumors in the DPEG-BPSi-1.0 + laser treatment group were cured. This significant antitumor efficacy in both DPEG-BPSi NPs with laser treatment groups ($P < 0.0001$, compared with control group) was also demonstrated by the tumor weight evolution (Figure 6a). The degree of apoptosis was then evaluated by TUNEL assay in CT 26 tumors. Being consistent with our in vivo antitumor efficacy results, tumors from DPEG-BPSi with laser irradiation-treated groups exhibited apoptosis of different levels; especially with the higher dosage treatment group, the apoptosis signals (number of nuclei in brown color) were of the greatest percentage and present some necrotic areas (Figure 6b). Also, we could found some apoptosis signals in control groups and other treatment groups without laser irradiation, which may be due to the large size of the tumors after 14 days resulting in the lack of sufficient nutrition sufficient.

Furthermore, changes in the animals' body weights were also investigated to evaluate the systemic toxicity of the treatments (Figure S11, Supporting Information). The statistical significance was determined with multiple t test using the Holm−Sidak method. In comparison to the control groups, there was no statistically significant change in the body weight ($P > 0.05$) within the treatment groups after 2 weeks, indicating no toxicity of nanoparticles with the applied dosage regimen. In addition, when compared with the control group, the nanoparticle-treated mice showed no significant organ lesions in H&E images (Figure S12), indicating that the DPEG-BPSi nanoparticles have a good biocompatibility for cancer treatments.

CONCLUSIONS

A scalable and high-yield method was developed to produce black mesoporous silicon nanoparticles with an exceptional ability to absorb infrared light and convert it into heat. The material was exploited for photothermal therapy of cancer in vivo with good success. The nanoparticles had a large mass extinction coefficient (13.2 L/g/cm) and a high photothermal conversion efficiency (33.4%). Their photothermal performance was comparable to, or even better than, that of the state-of-the-art materials like gold and carbon nanomaterials. Moreover, the developed black mesoporous silicon nanoparticles showed excellent biocompatibility and tunable biodegradability, thus facilitating their utilization in biomedical applications. The high surface area and mesoporous structure of the nanoparticles together with their inherent ability to absorb efficiently infrared radiation mean that the nanoparticles are an attractive platform for integration with different treatment modalities like synergistic chemotherapy/photothermal therapy and photothermal therapy/immunotherapy.

ASSOCIATED CONTENT

Supporting Information

The Supporting Information is available free of charge on the ACS Publications website at DOI: 10.1021/acsami.8b04557.

Temperature-controlled laser heating setup for in vitro cell tests, particle diameter distribution, calculation of porosity, XPS analysis of ePSi, Raman spectrum of bulk silicon wafer, UV−vis spectra of ePSi, different silicon species in XPS analysis, sample information in photothermal heating tests, the optical band gap calculation, TEM images, comparison of BPSi with gold nanoparticles in laser heating, photostability tests, effect of PEG coating on the heating performance of BPSi, calculation of photothermal conversion efficiency, thermogravimetric curves, ζ-potential, cell viability of CT 26 cells, two-dimensional plots of flow cytometry, body weight changes of mice, H&E images (PDF)

AUTHOR INFORMATION

Corresponding Authors

*E-mail: wujun.xu@uef.fi (W.X.).
*E-mail: xxfanny@fmmu.edu.cn (L.F.).
*E-mail: vesa-pekka.lehto@uef.fi (V.-P.L.).

ORCID

Wujun Xu: 0000-0002-3177-4709
Konstantin Tamarov: 0000-0003-0087-4878
Tuomo Nissinen: 0000-0002-4870-5101
Vesa-Pekka Lehto: 0000-0001-8153-1070

Author Contributions

[▽]W.X. and K.T. contributed equally to this work.

Notes

The authors declare no competing financial interest.

ACKNOWLEDGMENTS

The authors thank M.Sc. Maria-Viola Martikainen for her kind help with flow cytometry measurements. The Academy of Finland (Grant Nos, 314412 and 314552), Finnish Cultural Foundation (Pohjois-Savon Rahasto), and Magnus Ehrnrooth Foundation (Magnus Ehrnroothin Säätiö) are gratefully acknowledged for financial support. This work was partially funded by grants from the National Natural Science Foundation of China No. 81201179, the National Key Research and Development Program of China (2017YFC0107405), Natural Science Basic Research Plan in Shaanxi Province of China (2017JQ8049), and State Key Laboratory of Cancer Biology Open Fund (CBSKL201706). Authors also want to thank SIB Labs (University of Eastern Finland) for providing laboratory facilities and technical support.

REFERENCES

(1) Su, J.; Sun, H.; Meng, Q.; Yin, Q.; Zhang, P.; Zhang, Z.; Yu, H.; Li, Y. Bioinspired Nanoparticles with Nir-Controlled Drug Release for Synergetic Chemophotothermal Therapy of Metastatic Breast Cancer. *Adv. Funct. Mater.* **2016**, *26*, 7495−7506.

(2) Kang, S.; Lee, J.; Ryu, S.; Kwon, Y.; Kim, K.-H.; Jeong, D. H.; Paik, S. R.; Kim, B.-S. Gold Nanoparticle/Graphene Oxide Hybrid Sheets Attached on Mesenchymal Stem Cells for Effective Photothermal Cancer Therapy. *Chem. Mater.* **2017**, *29*, 3461−3476.

(3) Feng, L.; He, F.; Liu, B.; Yang, G.; Gai, S.; Yang, P.; Li, C.; Dai, Y.; Lv, R.; Lin, J. G-C3n4 Coated Upconversion Nanoparticles for 808 Nm near-Infrared Light Triggered Phototherapy and Multiple Imaging. *Chem. Mater.* **2016**, *28*, 7935−7946.

(4) Zou, L.; Wang, H.; He, B.; Zeng, L.; Tan, T.; Cao, H.; He, X.; Zhang, Z.; Guo, S.; Li, Y. Current Approaches of Photothermal Therapy in Treating Cancer Metastasis with Nanotherapeutics. *Theranostics* **2016**, *6*, 762−772.

DOI: 10.1021/acsami.8b04557
ACS Appl. Mater. Interfaces 2018, 10, 23529−23538

(5) Song, X.; Liang, C.; Gong, H.; Chen, Q.; Wang, C.; Liu, Z. Photosensitizer-Conjugated Albumin-Polypyrrole Nanoparticles for Imaging-Guided in Vivo Photodynamic/Photothermal Therapy. *Small* **2015**, *11*, 3932−3941.
(6) Sheng, Z.; Hu, D.; Zheng, M.; Zhao, P.; Liu, H.; Gao, D.; Gong, P.; Gao, G.; Zhang, P.; Ma, Y.; Cai, L. Smart Human Serum Albumin-Indocyanine Green Nanoparticles Generated by Programmed Assembly for Dual-Modal Imaging-Guided Cancer Synergistic Phototherapy. *ACS Nano* **2014**, *8*, 12310−12322.
(7) Jian, W.-H.; Yu, T.-W.; Chen, C.-J.; Huang, W.-C.; Chiu, H.-C.; Chiang, W.-H. Indocyanine Green-Encapsulated Hybrid Polymeric Nanomicelles for Photothermal Cancer Therapy. *Langmuir* **2015**, *31*, 6202−6210.
(8) Li, K.-C.; Chu, H.-C.; Lin, Y.; Tuan, H.-Y.; Hu, Y.-C. Pegylated Copper Nanowires as a Novel Photothermal Therapy Agent. *ACS Appl. Mater. Interfaces* **2016**, *8*, 12082−12090.
(9) Antaris, A. L.; Robinson, J. T.; Yaghi, O. K.; Hong, G.; Diao, S.; Luong, R.; Dai, H. Ultra-Low Doses of Chirality Sorted (6, 5) Carbon Nanotubes for Simultaneous Tumor Imaging and Photothermal Therapy. *ACS Nano* **2013**, *7*, 3644−3652.
(10) Shao, L.; Zhang, R.; Lu, J.; Zhao, C.; Deng, X.; Wu, Y. Mesoporous Silica Coated Polydopamine Functionalized Reduced Graphene Oxide for Synergistic Targeted Chemo-Photothermal Therapy. *ACS Appl. Mater. Interfaces* **2017**, *9*, 1226−1236.
(11) Wang, D.; Xu, Z.; Yu, H.; Chen, X.; Feng, B.; Cui, Z.; Lin, B.; Yin, Q.; Zhang, Z.; Chen, C.; Wang, J.; Zhang, W.; Li, Y. Treatment of Metastatic Breast Cancer by Combination of Chemotherapy and Photothermal Ablation Using Doxorubicin-Loaded DNA Wrapped Gold Nanorods. *Biomaterials* **2014**, *35*, 8374−8384.
(12) Cheng, X.; Sun, R.; Yin, L.; Chai, Z.; Shi, H.; Gao, M. Light-Triggered Assembly of Gold Nanoparticles for Photothermal Therapy and Photoacoustic Imaging of Tumors in Vivo. *Adv. Mater.* **2017**, *29*, No. 1604894.
(13) Chen, J.; Liang, H.; Lin, L.; Guo, Z.; Sun, P.; Chen, M.; Tian, H.; Deng, M.; Chen, X. Gold-Nanorods-Based Gene Carriers with the Capability of Photoacoustic Imaging and Photothermal Therapy. *ACS Appl. Mater. Interfaces* **2016**, *8*, 31558−31566.
(14) Liu, J.; Zheng, X.; Yan, L.; Zhou, L.; Tian, G.; Yin, W.; Wang, L.; Liu, Y.; Hu, Z.; Gu, Z.; Chen, C.; Zhao, Y. Bismuth Sulfide Nanorods as a Precision Nanomedicine for in Vivo Multimodal Imaging-Guided Photothermal Therapy of Tumor. *ACS Nano* **2015**, *9*, 696−707.
(15) Song, G.; Wang, Q.; Wang, Y.; Lv, G.; Li, C.; Zou, R.; Chen, Z.; Qin, Z.; Huo, K.; Hu, R.; Hu, J. A Low-Toxic Multifunctional Nanoplatform Based on Cu9s5@Msio2 Core-Shell Nanocomposites: Combining Photothermal- and Chemotherapies with Infrared Thermal Imaging for Cancer Treatment. *Adv. Funct. Mater.* **2013**, *23*, 4281−4292.
(16) Xu, W.; Riikonen, J.; Lehto, V.-P. Mesoporous Systems for Poorly Soluble Drugs. *Int. J. Pharm.* **2013**, *453*, 181−197.
(17) Xu, W.; Thapa, R.; Liu, D.; Nissinen, T.; Granroth, S.; Närvänen, A.; Suvanto, M.; Santos, H. A.; Lehto, V.-P. Smart Porous Silicon Nanoparticles with Polymeric Coatings for Sequential Combination Therapy. *Mol. Pharmaceutics* **2015**, *12*, 4038−4047.
(18) Hong, C.; Lee, J.; Zheng, H.; Hong, S.-S.; Lee, C. Porous Silicon Nanoparticles for Cancer Photothermotherapy. *Nanoscale Res. Lett.* **2011**, *6*, 321−328.
(19) Lee, C.; Kim, H.; Hong, C.; Kim, M.; Hong, S. S.; Lee, D. H.; Lee, W. I. Porous Silicon as an Agent for Cancer Thermotherapy Based on near-Infrared Light Irradiation. *J. Mater. Chem.* **2008**, *18*, 4790−4795.
(20) Sun, Z.; Xie, H.; Tang, S.; Yu, X. F.; Guo, Z.; Shao, J.; Zhang, H.; Huang, H.; Wang, H.; Chu, P. K. Ultrasmall Black Phosphorus Quantum Dots: Synthesis and Use as Photothermal Agents. *Angew. Chem.* **2015**, *127*, 11688−11692.
(21) Zhang, H.; Wu, H.; Wang, J.; Yang, Y.; Wu, D.; Zhang, Y.; Zhang, Y.; Zhou, Z.; Yang, S. Graphene Oxide-Bagdf 5 Nano-composites for Multi-Modal Imaging and Photothermal Therapy. *Biomaterials* **2015**, *42*, 66−77.
(22) Zuo, X.; Xia, Y.; Ji, Q.; Gao, X.; Yin, S.; Wang, M.; Wang, X.; Qiu, B.; Wei, A.; Sun, Z.; Liu, Z.; Zhu, J.; Cheng, Y.-J. Self-Templating Construction of 3d Hierarchical Macro-/Mesoporous Silicon from 0d Silica Nanoparticles. *ACS Nano* **2017**, *11*, 889−899.
(23) Liu, N.; Huo, K.; McDowell, M. T.; Zhao, J.; Cui, Y. Rice Husks as a Sustainable Source of Nanostructured Silicon for High Performance Li-Ion Battery Anodes. *Sci. Rep.* **2013**, *3*, No. 1919.
(24) Dai, F.; Zai, J.; Yi, R.; Gordin, M. L.; Sohn, H.; Chen, S.; Wang, D. Bottom-up Synthesis of High Surface Area Mesoporous Crystalline Silicon and Evaluation of Its Hydrogen Evolution Performance. *Nat. Commun.* **2014**, *5*, No. 3605.
(25) Xu, W.; Rytkönen, J.; Rönkkö, S.; Nissinen, T.; Kinnunen, T.; Suvanto, M.; Närvänen, A.; Lehto, V.-P. A Nanostopper Approach to Selectively Engineer the Surfaces of Mesoporous Silicon. *Chem. Mater.* **2014**, *26*, 6734−6742.
(26) Näkki, S.; Rytkönen, J.; Nissinen, T.; Florea, C.; Riikonen, J.; Ek, P.; Zhang, H.; Santos, H. A.; Närvänen, A.; Xu, W.; Lehto, V.-P. Improved Stability and Biocompatibility of Nanostructured Silicon Drug Carrier for Intravenous Administration. *Acta Biomater.* **2015**, *13*, 207−215.
(27) Wan, J.; Cai, W.; Meng, X.; Liu, E. Monodisperse Water-Soluble Magnetite Nanoparticles Prepared by Polyol Process for High-Performance Magnetic Resonance Imaging. *Chem. Commun.* **2007**, 5004−5006.
(28) Neiner, D.; Chiu, H. W.; Kauzlarich, S. M. Low-Temperature Solution Route to Macroscopic Amounts of Hydrogen Terminated Silicon Nanoparticles. *J. Am. Chem. Soc.* **2006**, *128*, 11016−11017.
(29) Qin, W.-J.; Yang, X.-B.; Lu, Y.-W.; Sun, J.; Kulinich, S. A.; Du, X.-W. Silicon Nanodisks Via a Chemical Route. *Chem. Mater.* **2008**, *20*, 3892−3896.
(30) Lin, J.-H.; Chiu, H.-C.; Lin, Y.-R.; Wen, T.-K.; Patil, R. A.; Devan, R. S.; Chen, C.-H.; Shiu, H.-W.; Liou, Y.; Ma, Y.-R. Electrical and Chemical Characteristics of Probe-Induced Two-Dimensional Siox Protrusion Layers. *Appl. Phys. Lett.* **2013**, *102*, No. 031603.
(31) Alfonsetti, R.; De Simone, G.; Lozzi, L.; Passacantando, M.; Picozzi, P.; Santucci, S. Siox Surface Stoichiometry by Xps: A Comparison of Various Methods. *Surf. Interface Anal.* **1994**, *22*, 89−92.
(32) Murphy, A. Band-Gap Determination from Diffuse Reflectance Measurements of Semiconductor Films, and Application to Photoelectrochemical Water-Splitting. *Sol. Energy Mater. Sol. Cells* **2007**, *91*, 1326−1337.
(33) Roper, D. K.; Ahn, W.; Hoepfner, M. Microscale Heat Transfer Transduced by Surface Plasmon Resonant Gold Nanoparticles. *J. Phys. Chem. C* **2007**, *111*, 3636−3641.
(34) Sun, C.; Wen, L.; Zeng, J.; Wang, Y.; Sun, Q.; Deng, L.; Zhao, C.; Li, Z. One-Pot Solventless Preparation of Pegylated Black Phosphorus Nanoparticles for Photoacoustic Imaging and Photothermal Therapy Of cancer. *Biomaterials* **2016**, *91*, 81−89.
(35) Tian, Q.; Hu, J.; Zhu, Y.; Zou, R.; Chen, Z.; Yang, S.; Li, R.; Su, Q.; Han, Y.; Liu, X. Sub-10 Nm Fe3o4@Cu2-Xs Core-Shell Nanoparticles for Dual-Modal Imaging and Photothermal Therapy. *J. Am. Chem. Soc.* **2013**, *135*, 8571−8577.
(36) Zhou, Z.; Sun, Y.; Shen, J.; Wei, J.; Yu, C.; Kong, B.; Liu, W.; Yang, H.; Yang, S.; Wang, W. Iron/Iron Oxide Core/Shell Nanoparticles for Magnetic Targeting Mri and near-Infrared Photothermal Therapy. *Biomaterials* **2014**, *35*, 7470−7478.
(37) Suk, J. S.; Xu, Q.; Kim, N.; Hanes, J.; Ensign, L. M. Pegylation as a Strategy for Improving Nanoparticle-Based Drug and Gene Delivery. *Adv. Drug Delivery Rev.* **2016**, *99*, 28−51.
(38) Park, J. H.; Gu, L.; Von Maltzahn, G.; Ruoslahti, E.; Bhatia, S. N.; Sailor, M. J. Biodegradable Luminescent Porous Silicon Nanoparticles for in Vivo Applications. *Nat. Mater.* **2009**, *8*, 331−336.
(39) Huang, P.; Lin, J.; Li, W.; Rong, P.; Wang, Z.; Wang, S.; Wang, X.; Sun, X.; Aronova, M.; Niu, G.; Leapman, R. D.; Nie, Z.; Chen, X. Biodegradable Gold Nanovesicles with an Ultrastrong Plasmonic Coupling Effect for Photoacoustic Imaging and Photothermal Therapy. *Angew. Chem., Int. Ed. Engl.* **2013**, *52*, 13958−13964.

DOI: 10.1021/acsami.8b04557
ACS Appl. Mater. Interfaces 2018, 10, 23529−23538

(40) Tong, L.; Zhao, Y.; Huff, T. B.; Hansen, M. N.; Wei, A.; Cheng, J.-X. Gold Nanorods Mediate Tumor Cell Death by Compromising Membrane Integrity. *Adv. Mater.* **2007**, *19*, 3136−3141.
(41) Hildebrandt, B.; Wust, P.; Ahlers, O.; Dieing, A.; Sreenivasa, G.; Kerner, T.; Felix, R.; Riess, H. The Cellular and Molecular Basis of Hyperthermia. *Crit. Rev. Oncol./Hematol.* **2002**, *43*, 33−56.

DOI: 10.1021/acsami.8b04557
ACS Appl. Mater. Interfaces 2018, 10, 23529−23538